Journal of Structural Geology, Vol. 14, No. 1, pp. 105 to 120, 1992
Printed in Great Britain

0191-8141/92 $05.00+0.00

Single layer buckle folding in non-linear materials—II. Comparison between theory and experiment

NEIL S. MANCKTELOW and MOHAMMAD R. ABBASSI

Geologisches Institut, ETH-Zentrum, CH-8092 Zürich, Switzerland

(*Received* 27 *September* 1990; *accepted in revised form* 23 *May* 1991)

Abstract—Results from scale-model experiments on the development of single layer folds from an initial perturbation of known shape are compared with infinitesimal amplitude theories for buckling of non-linear viscous materials. The experiments were performed in pure shear, using paraffin wax as an analogue for the power-law behaviour of common rocks. Effective viscosity ratios of 30 and 8 between layer and matrix were used, with power-law stress exponents of around 3.8 for the matrix and around 3 for the layer. The layer material shows strain softening behaviour. The variation of growth rate with wavelength (the range of wavelengths corresponding to the Fourier series representation for the non-periodic fold shape) was determined for each of the perturbation shapes and viscosity contrasts employed. These growth rate curves closely resemble those calculated from theory, but for short wavelengths and particularly for narrow initial pertubations, observed growth rates tend to be higher than theoretical values. This may reflect the strain softening behaviour of the layer. Bonding of the matrix–layer interface appears to have a much greater effect on the growth rate curve than theoretically predicted, at least for the low to moderate viscosity ratios investigated. Experimental fold shapes are also compared directly with theoretical shapes. The best-fit between theory and observation occurs for values of the viscosity ratio and the layer stress exponent which are very close to the calibrated material properties, providing further experimental evidence that current fold theories are a good approximation to low but finite amplitude, single layer folding in non-linear materials.

INTRODUCTION

FOLDS are perhaps the commonest and most obvious manifestation of deformation in layered or foliated rocks. The study of fold development is, therefore, fundamental to understanding orogenesis. Folds are of three broad genetic types (e.g. Hudleston 1986): passive folds, where the layer has no mechanical significance and amplification is purely kinematic (e.g. fault-bend and fault-propagation folds, Suppe 1983, Suppe & Medwedeff 1990; sheath and intrafolial fold development in shear zones, Cobbold & Quinquis 1980, fig. 11 from Van Den Driessche & Brun 1987), bending or flexural folds involving transverse forces acting on the layer (e.g. flexure of the lithosphere, Nadai 1963, pp. 131–146, Ranalli 1987, pp. 203–210) and buckle folds developed due to the mechanical instability of layered or anisotropic materials under compression (e.g. Biot 1961, Cobbold *et al.* 1971). The three folding mechanisms are not mutually exclusive: the growth of buckle folds, for example, is always accompanied by an additional kinematic component of amplification (e.g. Biot 1961, Smith 1975).

This study considers folds developed as the result of buckling instability when a single layer embedded in a weaker matrix is shortened parallel to the layer. Such folding is directly related to the material properties of the rocks involved and several field studies of single layer fold geometry have been made with the specific aim of estimating the rock rheology during folding (e.g. Sherwin & Chapple 1968, Hudleston 1973b, Fletcher 1974, Fletcher & Sherwin 1978, Hudleston & Holst 1984). These studies rely on theoretical results linking fold geometry, and in particular fold wavelength, to rheology. Two general approaches to the theory of buckle folding have been developed over the past 30 years: an approximate, linearized analytical solution for very low fold amplitudes (infinitesimal fold theories e.g. Biot 1961, 1965b, Ramberg 1961) and numerical simulations at finite amplitude (e.g. Chapple 1968, Dieterich 1969, Parrish 1973, Lewis & Williams 1978). Unfortunately, these theoretical results cannot be adequately tested by direct comparison with natural examples, as only the final fold shape can be measured, and more rarely, the amount of layer parallel shortening estimated (e.g. Sherwin & Chapple 1968, Hudleston & Holst 1984). As is more thoroughly discussed in Part I (Abbassi & Mancktelow 1992), the amplified fold geometry after finite strain may also be strongly influenced by the shape and position of initial irregularities in the layer, which, for natural folds, cannot be known with any accuracy. It will also depend on the material properties of the matrix and layer (i.e. their constitutive flow laws and possible anisotropy), the degree and homogeneity of bonding between matrix and layer, the thickness of the layer(s) and their separation, and the overall deformation history. Few of these parameters can be accurately determined for natural examples.

More detailed investigation is possible using scale models which employ analogue materials to simulate rock behaviour (e.g. Hubbert 1937, Ramberg 1961). The results of a series of experiments, which use paraffin wax as an analogue for rock with power-law viscous rheology (cf. Cobbold 1975, Neurath & Smith 1982, Mancktelow 1988), are presented and compared with corresponding results from theories of buckle folding in non-linear materials (Fletcher 1974, 1977, Smith 1977, 1979). Strictly speaking, the first-order approximations

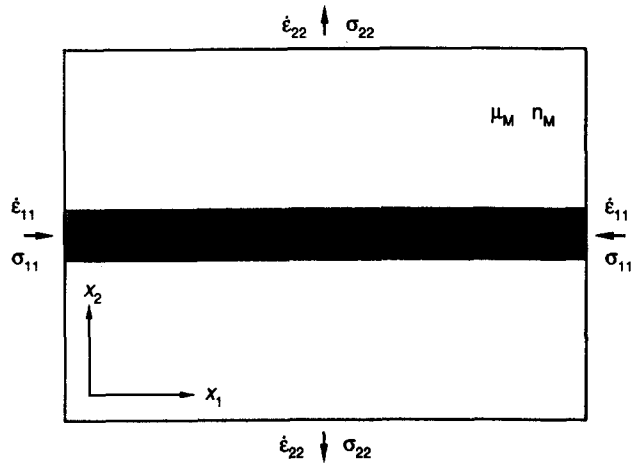

Fig. 1. Geometry of single layer folding in pure shear. The layer is aligned parallel to the x_1 axis, with thickness h, with viscosity in the basic unperturbed flow μ_L and with a stress exponent n_L; the corresponding values for the matrix are μ_M and n_M, respectively. The boundaries of the block are shortened parallel to the layer at a rate $\dot{\varepsilon}_{11}$. For constant volume, $\dot{\varepsilon}_{22} = -\dot{\varepsilon}_{11}$.

inherent in these linearized theories are only valid at infinitesimal fold amplitudes. Obviously, measurements on scale models and natural folds must be made on folds of finite amplitude. An important aim of this study is, therefore, to consider the proposal by Chapple (1968) that the results of these infinitesimal theories can be reasonably extrapolated to low but finite amplitudes, where fold limb dips do not exceed 15–20°. The current series of experiments allow comparison within this range and can also consider deviations away from theoretical behaviour as amplitude increases. These experimental observations are clearly important if measurements of natural fold geometry are to be used, via the theoretical relations, to obtain rheological information.

A very simple geometry is considered in the experiments, namely a single isolated layer within a homogeneous matrix deformed under conditions of pure shear, with the shortening direction parallel to the layer (Fig. 1). This geometry is similar to that employed in many previous experiments employing both elastic and viscous materials (e.g. Biot *et al.* 1961, Ramberg 1961, 1963, 1964a, Currie *et al.* 1962, Hudleston 1973a, Cobbold 1975, Neurath & Smith 1982) and is not unrealistic, as approximately symmetric single layer folds are fairly common in nature (Sherwin & Chapple 1968, Cobbold 1975, Hudleston & Holst 1984). Earlier experimental studies concerned specifically with the verification of buckle fold theories using reportedly linear viscous materials were performed by Biot *et al.* (1961) and Hudleston (1973a). Neurath & Smith (1982) carried out experiments in non-linear materials, using paraffin wax, to study the amplification rates of perturbations with known initial wavelengths for both folding and boudinage instabilities. The approach employed here is similar to that developed by Biot *et al.* (1961), where the development of a single isolated perturbation of known initial shape is monitored during progressive shortening of the layer. Such an approach allows the growth rate of a whole range of wavelengths (the Fourier components of the non-periodic fold shape developed from the initial irregularity) to be estimated from a single experiment.

THEORIES ON THE INITIATION OF BUCKLE FOLDING

Short summary of published theoretical results

The body of literature concerned with theoretical studies of buckle folding is very extensive (e.g. Biot 1957, 1959a,b,c, 1961, 1963, 1964a,b, 1965a,b,c, Ramberg 1959, 1960, 1961, 1963, 1964a,b, 1970a,b, 1981, Currie *et al.* 1962, Price 1967, Chapple 1968, 1969, Erzhanov & Egarov 1970, Treagus 1973, De Caprariis 1974, Fletcher 1974, 1977, Smith 1975, 1977, 1979, Johnson 1977, Kerr 1986) and a comprehensive review will not be attempted here. Only those results which are relevant for direct comparison with the experiments are summarized and the reader should return to the original papers for a detailed development.

The assumed initial geometry for the theoretical analysis of single layer buckle folding is as given in Fig. 1. The materials are taken to be non-linear viscous, with effective viscosity μ and stress exponent n defined as in Fig. 2, following Smith (1977, 1979, fig. 2). As discussed by, among others, Biot (1961, 1965b), Ramberg (1961), Fletcher (1974) and Smith (1975), an initial sinusoidal deflection $y(x)$ of the layer, as represented by

$$y(x) = y_0 \cos lx,$$

where l is the wavenumber, $l = 2\pi/L$, and L the wavelength, will increase exponentially with strain, such that after a logarithmic strain ε parallel to the layer, the deflection $y(x,\varepsilon)$ is given by

$$y(x,\varepsilon) = y_0 \exp[-(1+q)\varepsilon] \cos lx.$$

The negative sign in the exponent arises from the convention that shortening strain is negative. Layer parallel shortening is neglected in this simplified analysis, but will be discussed in some detail below (and included in a numerical solution) when finite strain effects are con-

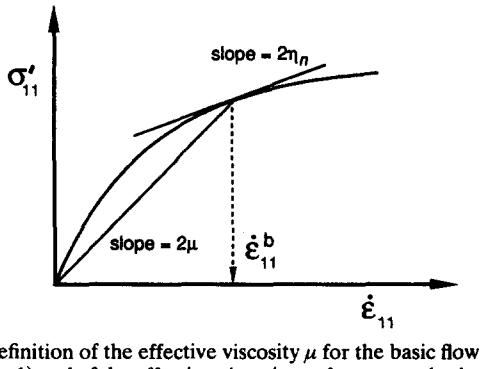

Fig. 2. Definition of the effective viscosity μ for the basic flow at rate $\dot{\varepsilon}^b_{11}$ (cf. Fig. 1) and of the effective viscosity η_n for a perturbation in the deviatoric normal stress, determined for a general non-linear viscous material from a plot of the deviatoric normal stress parallel to the x_1 axis (σ'_{11}) vs the corresponding longitudinal strain parallel to the same axis ($\dot{\varepsilon}_{11}$). The effective power-law stress exponent n is given by the ratio μ/η_n (Smith 1979).

sidered. The first term in the exponent (i.e. 1) describes the kinematic amplification of the perturbation during shortening. The second term q is the non-dimensional dynamic growth rate of the perturbation due to mechanical (buckling) instability (Smith 1977, Neurath & Smith 1982). The dynamic growth rate will be a function of the ratio of the effective viscosities of the layer μ_L and matrix μ_M

$$m = \frac{\mu_L}{\mu_M},$$

the power-law stress exponent of the layer n_L and of the matrix n_M, and the ratio of the wavelength L to the thickness of the layer h, which is expressed as the normalized wavenumber

$$s = hl = \frac{2\pi h}{L}.$$

All these quantities (m, n_L, n_M and s) are non-dimensional; it follows that any expression for the dynamic growth rate which utilizes only these quantities must also be non-dimensional.

Fletcher (1974) and independently Smith (1979) derived an expression for the dynamic growth rate of folds within a thick plate in the general case of non-linear materials, with complete adherence between the layer and matrix, which is given by:

$$q = \frac{2n_L\left(1 - \frac{1}{m}\right)}{\left\{-1 + Q^2 + \sqrt{n_L - 1} \times \frac{[(1+Q)^2 \exp(\alpha s) - (1-Q)^2 \exp(-\alpha s)]}{2\sin(\beta s)}\right\}} \quad (1)$$

where $\alpha = \sqrt{1/n_L}$, $\beta = \sqrt{1 - 1/n_L}$ and $Q = 1/m\sqrt{n_L/n_M}$. Plots derived from this equation for the maximum growth rate and the 'dominant wavelength' corresponding to this growth rate, over the range of material properties of interest in the current experiments, are presented in Fig. 3.

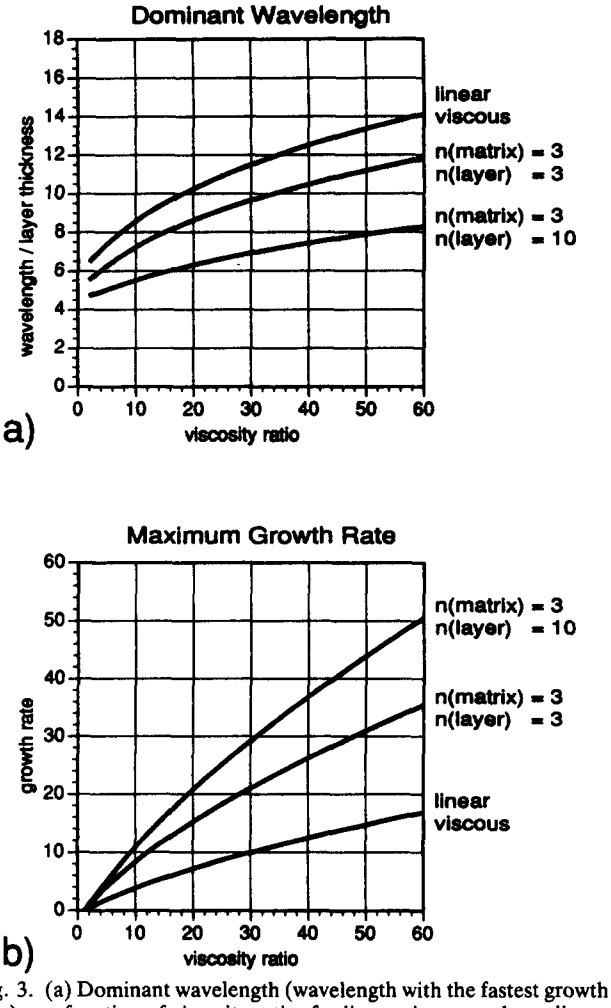

Fig. 3. (a) Dominant wavelength (wavelength with the fastest growth rate) as a function of viscosity ratio, for linear viscous and non-linear behaviour, with stress exponents n covering the range of interest for the experimental analogue materials. Plots are calculated using equation (1), as derived by Fletcher (1974) and Smith (1979). (b) Maximum dynamic growth rate, corresponding to dominant wavelength in (a) vs viscosity ratio. The total growth rate is obtained by adding a value of 1 for the additional kinematic component.

Effect of non-linear viscosity on single layer buckle folding

For an incompressible, Newtonian linear viscous material

$$\sigma'_{ij} = 2\mu\dot{\varepsilon}_{ij},$$

where σ'_{ij} is the deviatoric stress, $\dot{\varepsilon}_{ij}$ is the strain rate, and μ is a material parameter, the viscosity, dependent on temperature and pressure but not on σ'_{ij} and $\dot{\varepsilon}_{ij}$ (e.g. Biot 1965b, p. 376). Formally, *non-linear* (or *non-Newtonian*, or *effective*) viscosity is defined as

$$2\mu = \frac{\sigma'_{ij}}{\dot{\varepsilon}_{ij}} = f(\sigma'_{ij}) = f^*(\dot{\varepsilon}_{ij})$$

but one cannot determine *the* viscosity of a non-linear material, only the viscosity *at a given stress* (or strain rate) (Fig. 2) (e.g. Ranalli 1987, p. 79). The flow law relating deviatoric stress to strain rate reflects the physical properties of the material, and must be valid under any co-ordinate transformation. It is natural, therefore, to express it in terms of invariants, either of stress (e.g. Fletcher 1974, Schmeling 1987, Ranalli 1987, pp. 76–79) or strain rate (e.g. Smith 1977). As discussed by these authors, an important characteristic of non-linear viscosity, when considered in full tensorial form, is that a homogeneous isotropic material flowing due to some basic stress state will appear anisotropic to an additional small secondary or perturbation flow (see also Biot 1965b, pp. 89–95, Latham 1985). For small perturbations in deviatoric stress components which are already small (or zero) in the basic stress state, the change in the second stress invariant, and thus in the effective viscosity, will be negligible, so that the viscosity 'seen' by the stress perturbation is approximately linear. Perturbations in deviatoric stress components which are large in the original basic state will affect the second invariant (and thus the effective viscosity) to the full,

and the stress perturbation will see a non-linear viscosity with $\eta = \mu/n$ (Fig. 2). For a pure shear basic state as in Fig. 1, the effective perturbation viscosity for shear stress η_s will be approximately linear and equal to μ, the viscosity of the basic flow, whereas the effective perturbation viscosity for normal stress η_n is non-linear and given by μ/n. Thus $\eta_s/\eta_n = n$, and for strain rate softening materials such as paraffin (and rocks), the material is less viscous by a factor n for perturbations in normal stress than in shear stress. This has important implications for buckle folding, as it is exactly the opposite of the geometric anisotropy introduced due to the more viscous single layer lying parallel to the x_1 axis in Fig. 1 (Fletcher 1974, 1977, Smith 1977, 1979).

To discuss this effect of apparent or induced anisotropy in non-linear materials on single layer buckle folding, a simplified form of equation (1) will suffice. Much of the complexity of equation (1) is the result of secondary effects, due to the bending of a thick layer and to adherence between layer and matrix. These effects become significant only at low viscosity contrast and correspondingly short wavelengths (see below). If only the leading terms in the normalized wavenumber s are retained, the equation reduces to:

$$q \cong \frac{n_L}{\frac{n_L}{\sqrt{n_M}}\frac{1}{ms} + \frac{s^2}{12}} = \frac{\mu_L}{\frac{\mu_M}{\sqrt{n_M}}\frac{1}{s} + \frac{\mu_L}{n_L}\frac{s^2}{12}} \qquad (2)$$

(from Fletcher 1974, Smith 1979) and corresponds to the thin-plate approximation for perfect slip presented by Biot (1961). As demonstrated by Biot (1965b, pp. 418–419), who also derived a more exact thick-plate solution, this approximation is perfectly adequate when the viscosity ratio between layer and matrix is high (Fig. 4). The approximation is less acceptable for low viscosity ratios (<100), where the more exact, thick-plate solution always gives a lower growth rate of the fold instability at short wavelengths, with the result that the maximum growth rate occurs at longer wavelengths than for the thin-plate approximation.

As noted by Fletcher (1974) and Smith (1979), equation (2) can be obtained by a simple modification of the linear viscous result of Biot (1961). The introduction of non-linearity in itself does not change the basic mechanism of buckle folding (except perhaps for extreme non-linearity where $n_L > 20$, which is not relevant to the material properties of our experiments, cf. Smith 1979). The denominator of equation (2) describes the combined viscous resistance of the matrix (the first term) and the layer (second term) to folding. It can be obtained from the Biot (1961) equation by substituting the appropriate non-linear perturbation viscosities η for the linear viscosities μ in the original derivation (Biot 1965b, pp. 389–391, Fletcher 1974, Smith 1979). The perturbation strain in the matrix involves a mixture of stretch and shear: the appropriate viscosity is, therefore, the geometric mean of the viscosities for stretch and shear (Biot 1965b p. 211), namely

$$\sqrt{\eta_n^M \eta_s^M} = \frac{\mu_M}{\sqrt{n_M}}.$$

For the high viscosity, long wavelength conditions appropriate to equation (2), fibre strains are developed within the layer (i.e a coaxial strain history with the geometry of tangential longitudinal strain, cf. fig. 7-63 from Ramsay 1967). The effective perturbation viscosity for normal stresses alone ($\eta_n^L = \mu_L/n_L$) is, therefore, the appropriate value for the layer. The final result, as given by equation (2), demonstrates the most important effects of non-linear material behaviour on buckle folding. If the power-law stress exponent is >1 (the usual case of strain rate softening materials), then the fold growth rate is always increased (Fig. 3b). Because of the induced anisotropy (which leads to the $\sqrt{n_M}$ term), the influence of the power-law exponent is greater for the layer than for the matrix.

The dependence of growth rate on wavelength can be seen as a competition between the layer and matrix: bending strains within the layer increase with decreasing radius of curvature and hence with decreasing wavelength; the width of the zone of heterogeneous contact

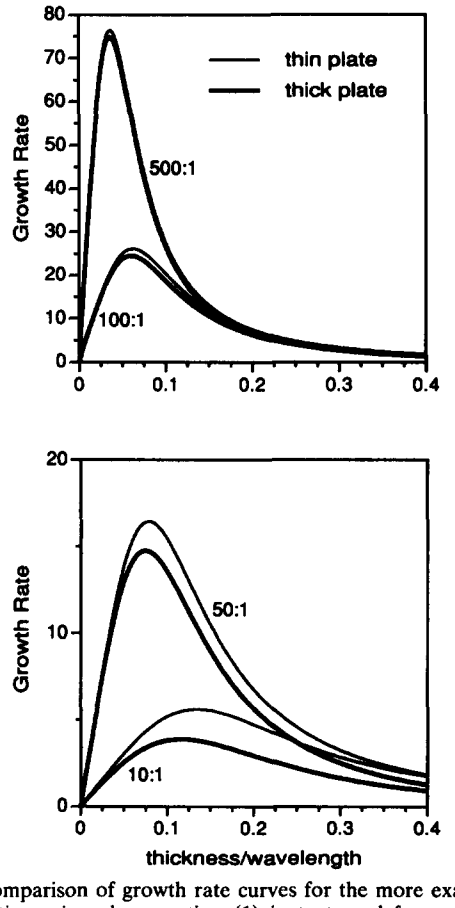

Fig. 4. Comparison of growth rate curves for the more exact thick-plate solution, given by equation (1) in text, and for a thin-plate approximation given by the much simpler equation (2), for various values of the viscosity ratio and for linear viscous behaviour of layer and matrix. For viscosity ratios greater than *ca* 100, the difference between thin- and thick-plate solutions is negligible.

strain in the adjacent matrix increases with increasing wavelength (e.g. Ramberg 1961). The relative rheological properties of layer and matrix will thus determine which wavelength represents the best compromise between the two competing effects. This will be the wavelength of fastest growth rate, or the so-called dominant wavelength (e.g. Biot 1961). For a strain rate softening rheology ($n > 1$), the effective perturbation viscosity for stretches in the layer due to bending is lower than in a linear material with the same viscosity for the basic flow, whereas the effect on the matrix (where both stretch and shear are involved) is less marked. Since the bending resistance of the layer to folding is reduced more than the resistance of the matrix, the dominant wavelength is shorter (Fig. 3a). In summary, the effect of non-linearity in rocks (and in paraffin) is greater for the layer than for the matrix, and results in an overall higher growth for buckle folding and a shorter dominant wavelength.

Effect of layer–matrix bonding

Biot (1959) explicitly considered the effect of the degree of bonding between layer and matrix in linear viscous materials and found that, for the thin-plate approximation, the growth rate is given by:

$$q = \frac{1}{\frac{1}{ms} + \frac{s^2}{12} + D}, \qquad (3)$$

where $D = 0$ for perfect slip and

$$D = \frac{1}{\frac{1}{4}\left(\frac{1}{1 + \frac{m}{s}}\right)}$$

for perfect adherence (no slip). The analysis was extended to the more exact thick-plate solution for the full range of possible slip conditions by Smith (1975, p. 1606)and his equation (41) for the growth rate of folds in linear viscous materials is graphed in Fig. 5 for the two extreme possibilities of no slip and perfect slip. It is immediately obvious that the distinction between slip and no-slip conditions becomes insignificant for high viscosity contrasts and that the effect of adherence is similar to that for a thick plate: namely, it decreases the growth rate at shorter wavelengths and shifts the maximum growth rate to slightly longer wavelengths.

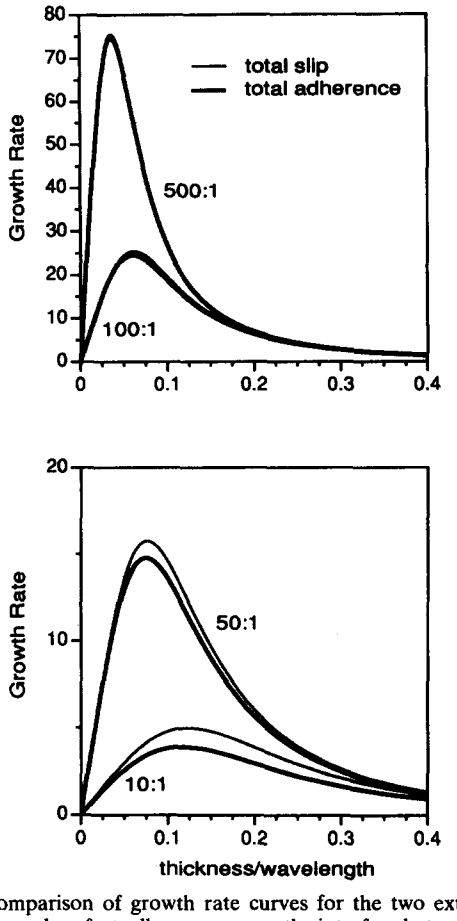

Fig. 5. Comparison of growth rate curves for the two extremes of perfect slip and perfect adherence across the interface between matrix and layer, for different values of the viscosity ratio and for linear viscous behaviour of layer and matrix, using the equation of Smith (1975). The difference between the two curves is only significant at low viscosity ratios (<*ca* 100), where adherence reduces the maximum growth rate and shifts it very slightly towards longer wavelengths.

THE AMPLIFICATION OF AN ISOLATED INITIAL PERTURBATION

Aims and limitations

Two approaches to the study of the amplification of initial irregularities in a single layer into finite amplitude folds are developed here. Both approaches rely on the fundamental assumption that fold shapes can be adequately represented by a Fourier series of sinusoidal components (see Appendix), and that, to a first-order approximation appropriate for low limb dips during fold initiation, individual Fourier components amplify independently of one another. The fold shape at any stage can be reconstructed by superposition of the amplified sinusoidal components. The two related approaches are as follows.

(1) To study the growth rates of individual Fourier components. The experimentally determined variation in growth rate with wavelength can then be compared to theoretical curves calculated using equation (1).

(2) To study the degree of fit between the theoretical fold shape obtained by amplification of the known initial shape with the observed shape during fold development. A least-squares method can be used to return the predicted material properties which best reproduce the observed shape. These predicted material properties can be compared with the calibrated values for the model materials. The quality of the fit between the theoretical and observed fold shape tests whether the results of infinitesimal amplitude fold theories may be usefully extrapolated to the amplitudes at which fold shapes can be accurately measured. The fit between predicted and measured material properties also tests the potential application of infinitesimal fold theories for

extracting rheological information from the shape of finite amplitude natural folds.

Basic theory

The method employed here closely follows that suggested by Biot *et al.* (1961) for buckle folding in linear elastic and linear viscous materials. The method introduces an initial perturbation of known mathematical form, and follows its development with increasing bulk shortening parallel to the layer. The geometry chosen is that of a bell-shaped curve:

$$y(x) = \frac{b}{1 + \left(\frac{x}{a}\right)^2} \tag{4}$$

which can be written as a Fourier integral:

$$\frac{b}{1 + \left(\frac{x}{a}\right)^2} = ab \int_0^\infty e^{-al} \cos lx dl. \tag{5}$$

As discussed above, a single, perfectly sinusoidal initial perturbation of the form $y(x) = y_0 \cos lx$ will be amplified, as the result of a finite shortening ε parallel to the layer, to a form given by $y(x,\varepsilon) = y_0 \exp[-(1 + q)\varepsilon] \cos lx$. For an initial deflection which is not perfectly sinusoidal, but localized, the problem can be approached using the principle of superposition, where the initial deflection is represented as the superposition of cosine functions by a Fourier integral. For any given wavenumber, each sinusoidal component under the integral sign is multiplied by the amplification factor $e^{-(1+q)\varepsilon}$. The deflection $y(x,\varepsilon)$ after strain ε is then obtained by summation (≡integration) of all the amplified components, namely

$$y(x,\varepsilon) = ab \int_0^\infty e^{-al-(1+q)\varepsilon} \cos lx dl.$$

This expression can be rewritten in a non-dimensional form using the normalized wavenumber s defined above:

$$\frac{y(x,\varepsilon)}{b} = \frac{a}{h} \int_0^\infty e^{-as/h-(1+q)\varepsilon} \cos\left(\frac{sx}{h}\right) ds. \tag{6}$$

Numerical integration and comparison with previous results

An efficient method for numerical computation of integrals of this type was first proposed by Filon (1928) and discussed in the appendix of Biot *et al.* (1961). This method is also used here, and has been checked against the slower but more traditional method of Simpson's rule (using routine QSIMP from Press *et al.* 1986) for the simple case of linear material behaviour. The size of the discrete steps for the numerical approximation was chosen such that the normalized $y(x,\varepsilon)$ is accurate to within 10^{-3}, which is more than sufficient for comparison with the experimental results. Results of the integration (which completes within seconds on an Apple Macintosh II personal computer) are identical to those published by Biot *et al.* (1961, fig. 3). As can be seen from Fig. 6, even for a very large and completely unrealistic total amplification (e.g. at $\varepsilon = 0.25$, see below), the fold train shape still diminishes quite rapidly in amplitude away from the amplitude maximum position at the origin, and the influence of the initial isolated perturbation is clearly discernible.

Limitations due to finite amplitude effects

The infinitesimal-amplitude treatment cannot be directly extrapolated to large amplitudes, as three assumptions restrict it to very low dip (Chapple 1968):

(1) the boundary between the layer and the medium is treated as a plane when calculating the stress distribution in the medium;

(2) if θ is the dip of the layer, it is assumed that $\sin\theta = \tan\theta = \theta$ at all points along the layer;

(3) and the distinction between arc length along the layer and distance parallel to the co-ordinate axis (i.e. the compression axis) is neglected, which implies that the strain rate in the layer ($\dot{\varepsilon}_{11}^{L}$) is identical to the strain rate in the adjacent matrix ($\dot{\varepsilon}_{11}^{M}$) and to that applied at the boundaries ($\dot{\varepsilon}_{11}$) (cf. Fig. 1).

The approach of Biot *et al.* (1961), in which the initial growth rate as a function of wavenumber is maintained to finite strains (up to $\varepsilon = 0.25$, Fig. 6), results in several major inconsistencies due to the neglect of these restrictions implicit in the infinitesimal-amplitude treatment. These will now be discussed in turn.

(a) The folds develop as a sum of sinusoidal Fourier components which increase in amplitude relative to fixed co-ordinates parallel to the compression axis (the x axis in our equations). This is clearly unrealistic as the

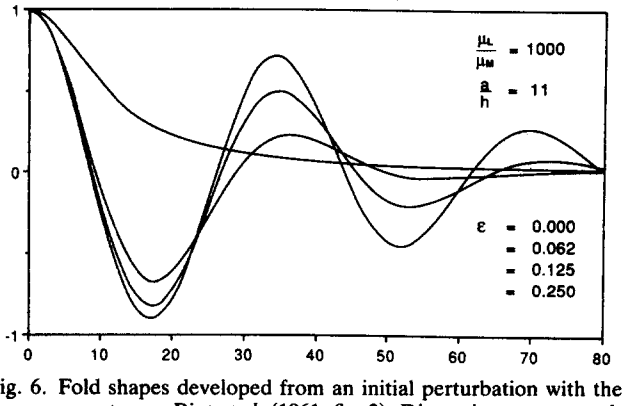

Fig. 6. Fold shapes developed from an initial perturbation with the same parameters as Biot *et al.* (1961, fig. 3). Dimensions are normalized against layer thickness h. For the initial bell-shaped perturbation, $a = 11$ and $b = 1$. The maximum amplitude (at $x = 0$) is always normalized to 1, as in the original paper by Biot *et al.* (1961). The viscosity ratio between matrix and layer is 1000 and the materials are assumed to be linear viscous. At such high viscosity ratios, the equation of Biot (1961), which employs a thin-plate approximation and a slipping layer–matrix interface, is effectively identical to the more complex equation (1) of Fletcher (1974) and Smith (1979), which is a more exact thick-plate solution for a non-slipping interface (see Figs. 4 and 5). The fold shapes derived from the two alternative equations are indistinguishable.

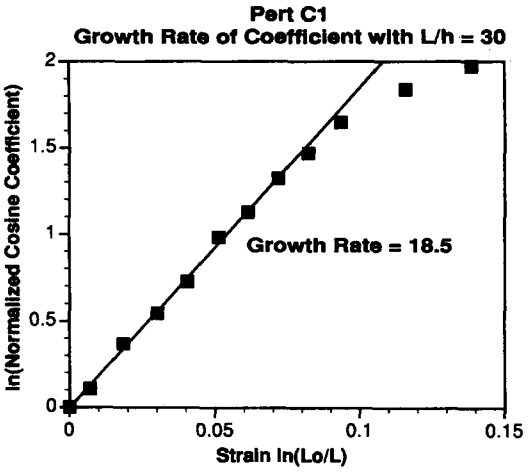

Fig. 7. ln(Fourier cosine coefficient) vs −(logarithmic strain) for the coefficient with wavelength 30 times layer thickness (layer thickness/wavelength = 0.033) from the right side of the fold in experiment Pert C1. The cosine coefficient has been normalized against the initial value in the introduced perturbation. Note the good linear fit up to natural strains of *ca* 0.08 (≈7.7% shortening), which corresponds to a limb dip of *ca* 20°.

kinematic component of the bulk deformation will produce a progressive shortening in the x-direction.

(b) The maintenance of constant growth rates to such high values of total shortening results in impossibly large amplification of the fold components: in the case recalculated from Biot *et al.* (1961) as presented in Fig. 6, the amplification of the central antiform would be of the order of 10^{14} at $\varepsilon = 0.25$. To obtain such amplification without near vertical limb dips and an enormous increase in the arc length of the layer demands that the initial irregularities be less than $\sim 10^{-13}$ of the layer thickness. For a 1 cm thick layer, this would require that all such initial irregularities were several orders of magnitude less than the size of individual atoms. It is clear, then, that the initial growth rates cannot be maintained to such large total amplifications and must decrease dramatically as folds grow (Fig. 7) (Neurath & Smith 1982, Abbassi & Mancktelow 1990). This change appears to occur at around 15–20° limb dip (Chapple 1968, Hudleston 1973a, Abbassi & Mancktelow 1992).

(c) The method also requires that the principle of superposition applies. Each Fourier component is amplified at a rate dependent on its wavenumber and independent of any other component; the final form of the wave train is found from the addition of these amplified components. Chapple (1968) found in his finite amplitude simulations that this assumption only held for limb dips <15–20°, which is confirmed by the current analogue experiments (see Fig. 7).

The approach of Biot *et al.* (1961) to the development of an isolated perturbation into a fold train with increasing shortening clearly cannot be pursued to such high finite strains as in their original paper. It may be a reasonable approximation for fold limb dips less than about 15–20° (e.g. Chapple 1968). Even within this range, however, the effect of layer parallel shortening should be considered (e.g. Fletcher 1974). The normalized wavenumber is $s = lh$, but now both the layer thickness h and the wavenumber l vary during the folding history. The approach used here is to divide the finite strain into a series of discrete small steps ($i = 1 \ldots n$, with a value of $\Delta\varepsilon_i = -0.02$) and to sum the growth rate over this series. The change in layer thickness with bulk shortening is known directly from measurements for each experiment (cf. Part I, Abbassi & Mancktelow 1992), and can be represented as a smooth spline curve through the data points. This gives the value of h_i for each value of the bulk strain ε. The value of the wavenumber l_i for each value of ε is given by $l_i = l_0 \exp(-\varepsilon)$ (remembering that ε is negative for shortening). For each step, the value $s_i = l_i h_i$ can then be substituted in equation (1) to obtain q_i. The value $q\varepsilon$ (the total dynamic amplification at strain ε) is then given by the series summation $\Sigma_{i=1}^{n} q_i \Delta\varepsilon_i$ and this value can be directly substituted into equation (6). Equation (6) returns the y co-ordinates of the fold shape relative to x co-ordinates defined in the undeformed initial state. In the original infinitesimal treatment, the distinction between the x co-ordinates in deformed and undeformed states was insignificant. For an extension to finite total shortening, however, the x co-ordinates must be shortened by the appropriate amount (corresponding to ε) to allow direct comparison with the photographed and digitized experimental folds.

EXPERIMENTAL METHOD

Material properties

Full details of the experimental conditions, methods and material calibrations are given in Part I (Abbassi & Mancktelow 1992). For the selected experimental conditions, the paraffin waxes used as modelling materials have an elastic–non-linear viscous rheology with a power-law relationship between flow stress and strain rate. The wax of melting range 46–48°C employed as the matrix flows in steady-state, with a stress exponent n of around 3.8 (Part I, fig. 2). The stiffer wax of melting range 58–60°C used to construct the single layers is strongly work softening under the same conditions, with a strain sensitivity $\kappa \approx 3$ (Part I, fig. 3), and a stress exponent of about 3 (Part I, fig. 4). Neurath & Smith (1982) have discussed the possible influence of strain softening on single layer buckling instability. The parameter ε^*, which they introduced as a measure of the strain softening behaviour, is equivalent to $1/\kappa$ from the current calibrations. Neurath & Smith (1982, p. 226) conclude that, to a first-order approximation, the combined effect of strain and strain rate softening can be characterized by defining an effective stress exponent n_{eff}, such that

$$\frac{1}{n_{\text{eff}}} \equiv \frac{1}{n} - \frac{\kappa}{2q} \qquad (7)$$

(allowing for the plane strain geometry of our calibration experiments; the calibrations of Neurath &

Smith 1982, were performed with an axial shortening geometry). The effective exponent n_{eff} will be dependent on the growth rate q of the particular wavelength component. With the calibrated values obtained for the 58–60°C melting range wax, the effective exponent n_{eff} would be 3.3 for $q = 50$, 5.5 for $q = 10$, 30 for $q = 5$, infinite for $q = 4.5$ and negative for $q < 4.5$! The relationship (7) is not very useful for direct application to the numerical simulation of fold amplification, as outlined above, since $q = f(n_L)$ (equation 1) but now, as the result of strain softening, the effective n_L should itself be a function of q. Qualitatively, however, equation (7) indicates that strain softening of the layer during buckle folding may result in an effective stress exponent which is higher than the directly calibrated value. The effect should be most marked for folds (or the wavelength components of fold shapes) with slow growth rates. This will become important below in the discussion of growth rates and material rheology as estimated from the experimental fold shapes.

As discussed above, for non-linear materials there is no single viscosity, only an effective viscosity for a particular basic state of stress or strain rate. All experiments and calibrations were performed under the same conditions (with constant strain rate of 3×10^{-5} s^{-1}) which represent this basic state. Because the layer strain softens, however, the viscosity ratio between layer and matrix also decreases with increasing strain. The maximum value corresponds to the ratio between the yield stress of the stiffer layer and the steady state flow stress of the matrix and is approximately 30:1 (fig. 1 from Part I, Abbassi & Mancktelow 1992). One experimental run was also performed in which the layer was constructed of a mixture of the two wax types, to obtain a lower ratio of around 8:1.

Initial geometry

An attempt was made to introduce initial isolated perturbations which resembled the theoretical bell-shaped curve as closely as possible. Moulds were produced on a numerically driven lathe where the mathematical shape could be predetermined. The amplitude of the perturbation (i.e. b) was always 2 mm such that, for a layer thickness of 4 mm, the initial normalized amplitude was 0.5. Three different moulds with a = 5.09, 10.19 and 20.37 mm gave initial average wavelengths of 8, 16 and 32 times layer thickness respectively and corresponding initial limb dips of 12°, 5° and 3° (see Part I, Abbassi & Mancktelow 1992). In manufacturing individual models, slight inaccuracies were unavoidable and the actual values of a and b for the models, rather than the moulds, were always determined using a least-squares best-fit of the equation for each side of the perturbation independently. These calibrated values were then used as the input for the numerical simulations. Duplicate experiments of each perturbation shape were performed to check reproducibility.

To analyse fold shape development, the median line of the initial and deformed layer was digitized and mathematically smoothed using a tight spline routine to minimize the scatter, of the order of 0.05 mm, introduced by manual digitizing (Panozzo 1988).

COMPARISON BETWEEN EXPERIMENT AND THEORY

Growth rates

The growth rates of particular wavelength (or more conveniently wavenumber) components are determined in three steps.

(1) The coefficients of the Fourier transform are calculated for the fold shape at different stages in the shortening history.

(2) The growth-rates for each of the cosine components are then determined by least-squares linear regression of a plot of the natural logarithm of the cosine coefficient vs the bulk shortening parallel to the layer (as logarithmic strain). These plots are only linear at low fold amplitudes corresponding to low limb dips (<*ca* 20°, Fig. 7). For higher limb dips, the growth rate progressively decreases (Fig. 7) and the independence of individual wavelength components is not maintained (Chapple 1968). The quality of the growth-rate data diminishes as the amplitude of the component in the initial introduced perturbation decreases; comparisons are then being made between very small quantities with large uncertainties. For each initial perturbation shape, there is a lower limit to the wavelengths on which reliable growth-rate data can be obtained.

(3) Finally, the growth-rate data for left and right sides of the fold strain and for duplicate experiments are averaged, and the average value (with error bars corresponding to the standard error) is plotted against the inverse of normalized wavelength for comparison with theoretical growth curves (equation 1 above).

The results for the series of experiments with a viscosity contrast of 30:1 and an easy-slip interface between matrix and layer are presented in Fig. 8. Considering the inaccuracies and assumptions in the several steps leading to the derivation of these plots, the fit between experiment and theory is quite good. For the narrow (Pert A) and intermediate (Pert B) width perturbations, the material properties corresponding to the best-fit theoretical curves are very close to the calibrated values for the materials employed. For the broadest initial perturbation (Pert C), the best fit occurs for a viscosity ratio (≈47) which is somewhat higher than the calibrated value of 30.

The major discrepancy between the shape of the experimentally estimated growth curves and the theoretical curves occurs at short wavelengths (i.e. large layer thickness/wavelength, Fig. 8), as is seen most clearly as the initial perturbation becomes narrower and these short wavelength components become more significant in the overall fold shape (Figs. 8a & b). The growth rate of the short wavelengths is consistently higher than predicted theoretically. It could be that this observation

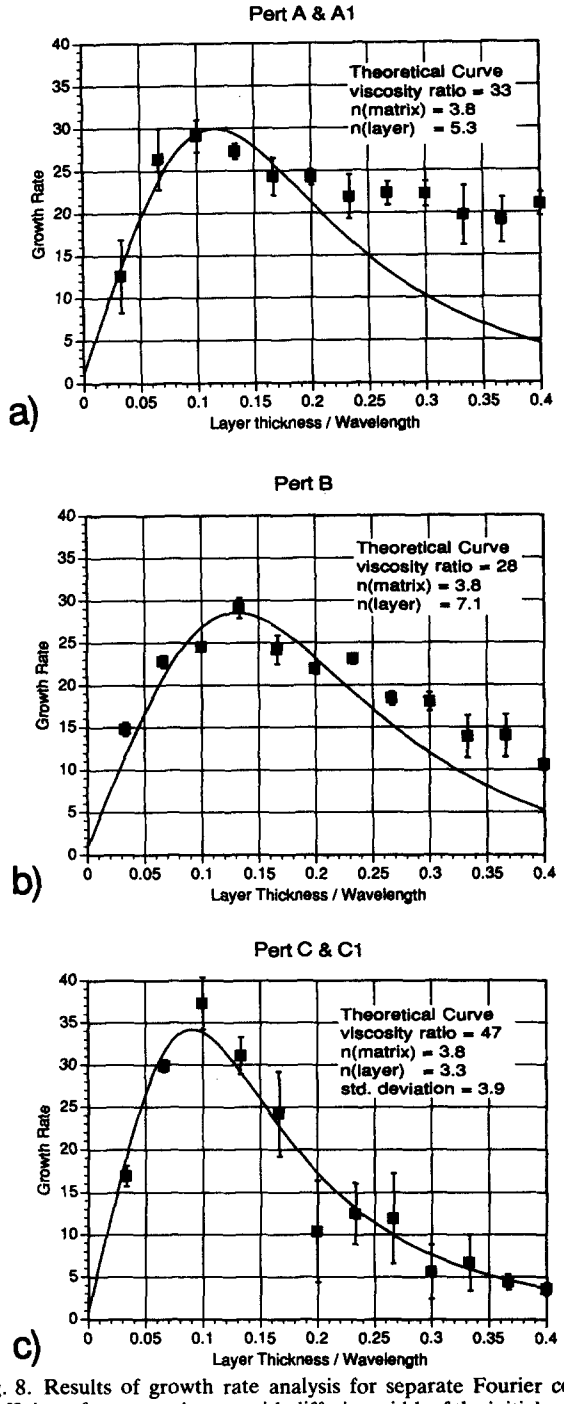

Fig. 8. Results of growth rate analysis for separate Fourier cosine coefficients from experiments with differing width of the initial perturbation but the same material properties, with a viscosity ratio of *ca* 30. Growth rates are plotted against the inverse normalized wavelength (thickness/wavelength = $2\pi s$, where s is the normalized wavenumber). Each plotted point represents the average of all determinations (left and right sides of the fold train giving two values per experiment, four values for duplicate runs) and error bars represent the standard errors. In each case, the theoretical curve is a least-squares best-fit for a fixed n_M exponent in the matrix of 3.8. (a) Results for the narrowest perturbation of initial average wavelength 8 times layer thickness. Duplicate experiments gave a total of four values which are averaged for each plotted point. The theoretical curve is a best-fit to the first six data points only. (b) Results for the intermediate perturbation of initial average wavelength 16 times layer thickness. The theoretical curve is a best-fit to the first six data points only. (c) Results for the broadest perturbation of initial average wavelength 32 times layer thickness. Duplicate experiments gave a total of four values which are averaged for each plotted point. The theoretical curve is a best-fit to all data points, with a standard deviation of 3.9. Note that at layer thickness/wavelength values greater than 0.15, the error bars are generally larger than in (a) and (b). This reflects the very low values of these short wavelength components in the original broad perturbation.

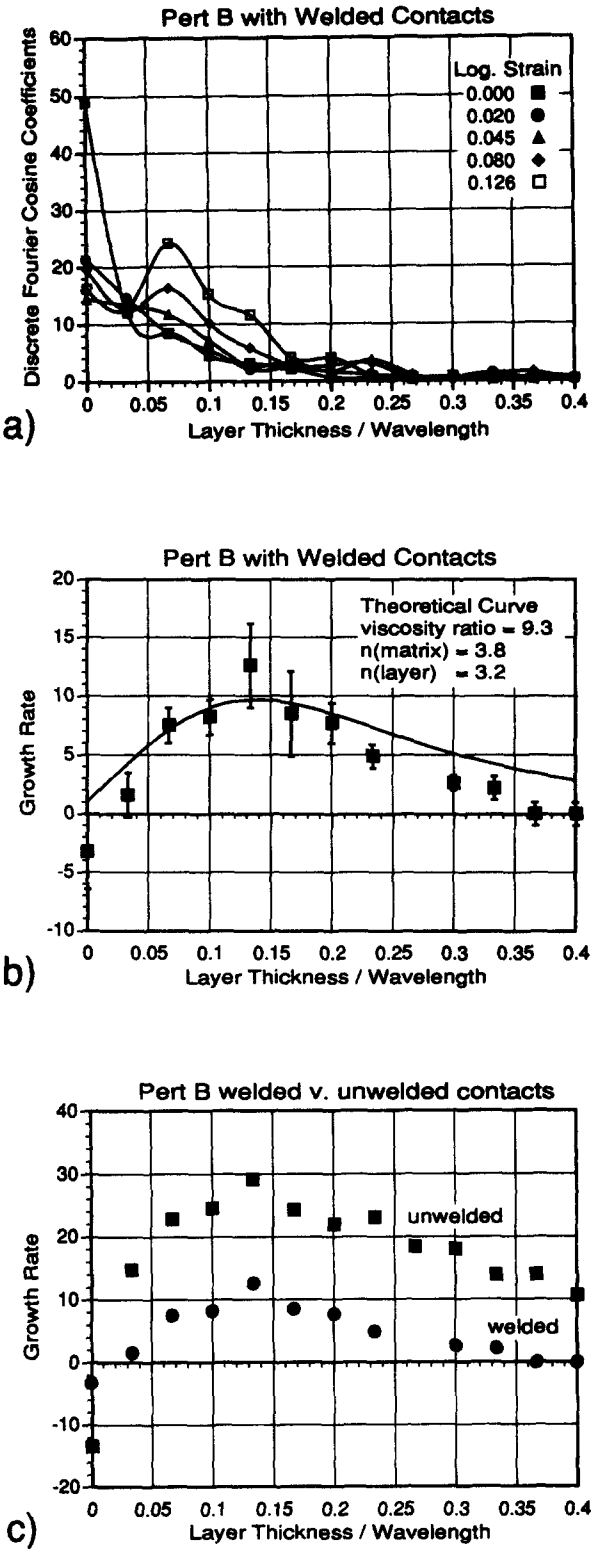

Fig. 9. Results of growth rate analysis for separate Fourier cosine coefficients from the experiment with a welded layer–matrix interface. Initial perturbation geometry and material properties are the same as for Pert B in Fig. 8. (a) Cosine coefficients of the discrete Fourier series for the right-hand side of the central antiform with increasing logarithmic strain ε. (b) Growth rate vs inverse normalized wavelength determined from the cosine coefficients for both sides of the central antiform. The error bars represent the standard error for the two values. The solid curve is a best-fit (in the range $0 <$ layer thickness/wavelength ≤ 0.2) theoretical growth rate curve, taking the calibrated value of 3.8 for the stress exponent of the matrix, and using equation (1) from Fletcher (1974). (c) Comparison of growth rate curves for experiments which were identical except for the degree of bonding of the layer–matrix interface. The growth rate curve for the unwelded experiment is that for Pert B in Fig. 8(b).

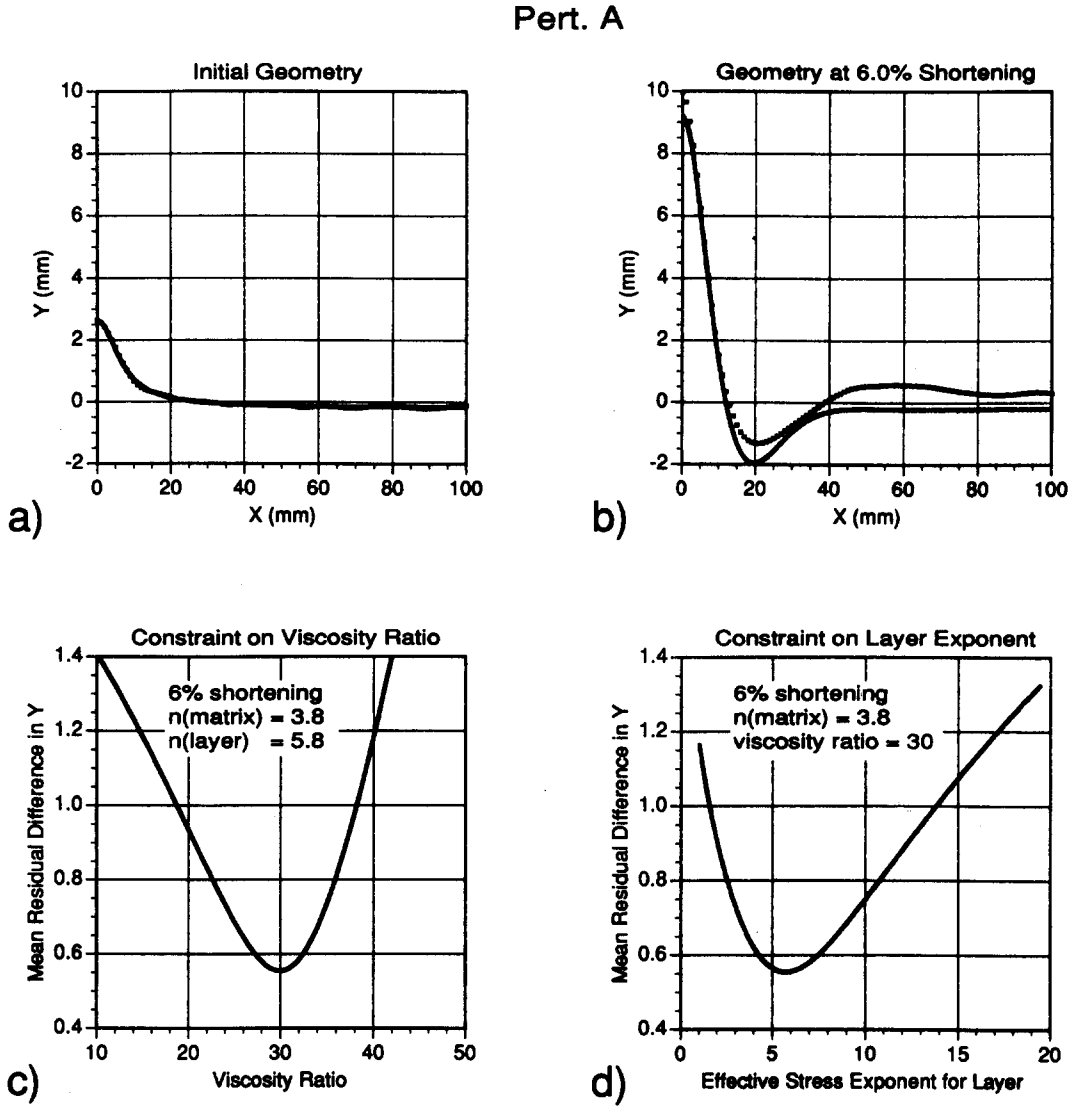

Fig. 10. Results of the best-fit shape analysis for the right side of the fold in experiment Pert A, with an initial average wavelength to the perturbation of 8 times layer thickness. (a) Digitized initial shape (points) and best-fit bell-shaped curve (solid line). The degree of fit is so good that digitized points are largely obscured by the bell curve, even though there is marked vertical exaggeration. (b) Digitized fold shape (points) and best-fit theoretical shape (line) at 6% shortening. (c) Mean residual difference in the Y co-ordinate (in mm) between theoretical prediction and the observed experimental shape as a function of the viscosity ratio used in the numerical calculation. The minimum value is tightly constrained around 30, which is also the calibrated value. (d) Mean residual difference in the Y co-ordinate (in mm) between theoretical prediction and the observed experimental shape as a function of the stress exponent for the layer used in the numerical calculation. The minimum value is tightly constrained at around 6. The calibrated value is *ca* 3, but if the effect of strain softening behaviour is considered, a higher effective stress exponent is predicted theoretically (Neurath & Smith 1982).

is due to the strain softening properties of the stiff layer. As discussed above, Neurath & Smith (1982) suggest that the behaviour of strain softening materials can be approximated by invoking an effective stress exponent n_{eff}, which is dependent both on the rate of strain softening and on the growth rate itself. This considerably complicates the determination of a theoretical growth curve such as in Fig. 8, as each Fourier component would have a different value of n(layer) corresponding to its specific growth rate. In particular, the n_{eff} value should increase for components with a slower growth rate, which in turn will tend to increase the growth rate itself, such that the growth rate should not decrease so rapidly towards shorter wavelengths. This is exactly what is observed in Fig. 8 for the strongly strain softening stiff layer. Clearly this effect can only be fully considered when similar experiments are available for materials which flow in steady state (i.e. no strain softening).

The results of a similar Fourier analysis of the growth rate of the experiment with a welded interface between layer and matrix are presented in Fig. 9. The effect of bonding is quite dramatic and results in a growth curve more consistent with a layer to matrix viscosity ratio of around 9–10 than with the calibrated value of 30. As is seen from the comparison between welded and unwelded experiments in Fig. 9(c), the growth rate for all wavelength components is lowered and the effect of bonding is much more dramatic than that predicted by the linear viscous infinitesimal theories as presented in

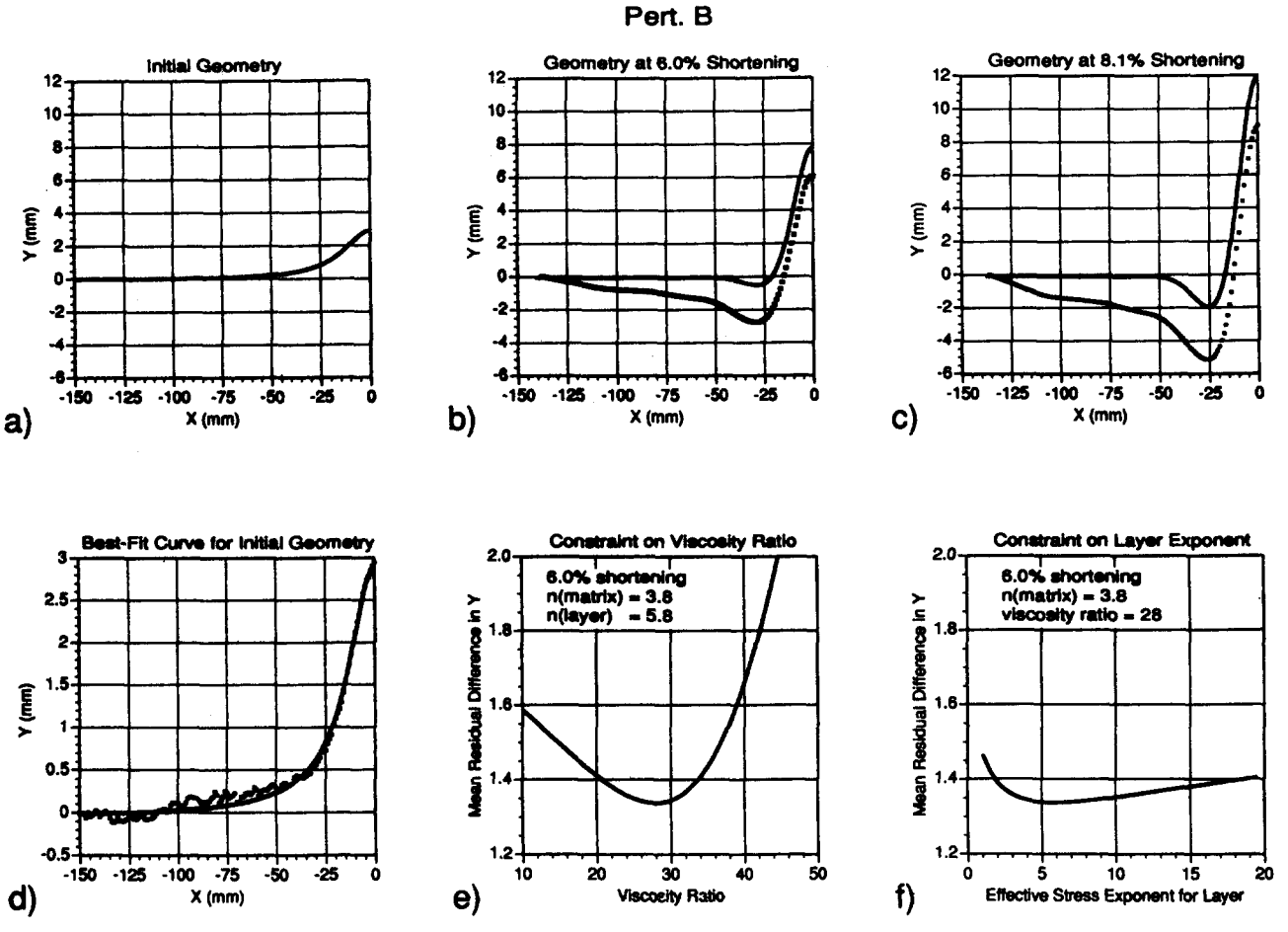

Fig. 11. Results of the best-fit shape analysis for the left side of the fold in experiment Pert B, with an initial average wavelength to the perturbation of 16 times layer thickness. (a) Best-fit bell-shaped curve to the introduced perturbation. (b) Digitized fold shape (points) and best-fit theoretical shape (line) at 6% shortening. (c) Digitized fold shape (points) and best-fit theoretical shape (line) at 8% shortening. (d) Digitized initial shape (points) and best-fit bell-shaped curve (solid line). Note that the degree of fit is excellent, even with the very marked vertical exaggeration of the plot. (e) Mean residual difference in the Y co-ordinate between theoretical prediction and the observed experimental shape as a function of the viscosity ratio used in the numerical calculation. Bulk shortening is 6%, corresponding to (b). The minimum value is well constrained around 28, which is close to the calibrated value of 30. (f) Mean residual difference in the Y co-ordinate between theoretical prediction and the observed experimental shape as a function of the stress exponent for the layer used in the numerical calculation. Bulk shortening is 6%, corresponding to (b) and (e). The minimum value is weakly constrained at around 6, which is the same value obtained in Fig. 10(d).

Fig. 5. As discussed in Part I (Abbassi & Mancktelow 1992), there is some risk that the construction procedure for the welded model may have altered the material properties of the matrix adjacent to the layer (by diffusion or by change in microstructure due to recrystallization) and further studies with different analogue materials are necessary to confirm this dramatic influence of the degree of layer–matrix bonding on folding with low to moderate viscosity ratios.

Fold shape comparison

As introduced above, the predicted deflection of the layer y is a function of x, the logarithmic strain ε and the growth rate q, where q is itself a function of the viscosity ratio m and the power law exponents of the layer and matrix n_L and n_M respectively. The method employed calculates the mean residual difference in the y co-ordinates, i.e.

$$\sqrt{\left(\sum_{x=0}^{T} [y_{\text{measured}} - y_{\text{calculated}}]^2/\text{number of data}\right)},$$

where T is the length of the digitized layer. The two sides of the perturbation about the origin $x = 0$ are treated independently and the perturbation is not assumed to be perfectly symmetric. Plots of this sum of residuals vs m and n_L are given in Figs. 10–12 for each of the initial perturbation shapes with calibrated $m = 30$ and in Fig. 13 for the experiment with $m = 8$. The power-law exponent of the matrix n_M has only limited influence on the growth rate q (Fletcher 1974) and is, therefore, not well constrained in the analysis; a value of 3.8 was assumed, as determined by the calibration experiments.

The least difference between observed and numerically predicted shape occurs for values of the material properties m and n_L which are very close to the experimentally calibrated values. This demonstrates that the theoretical approach outlined by Biot *et al.*

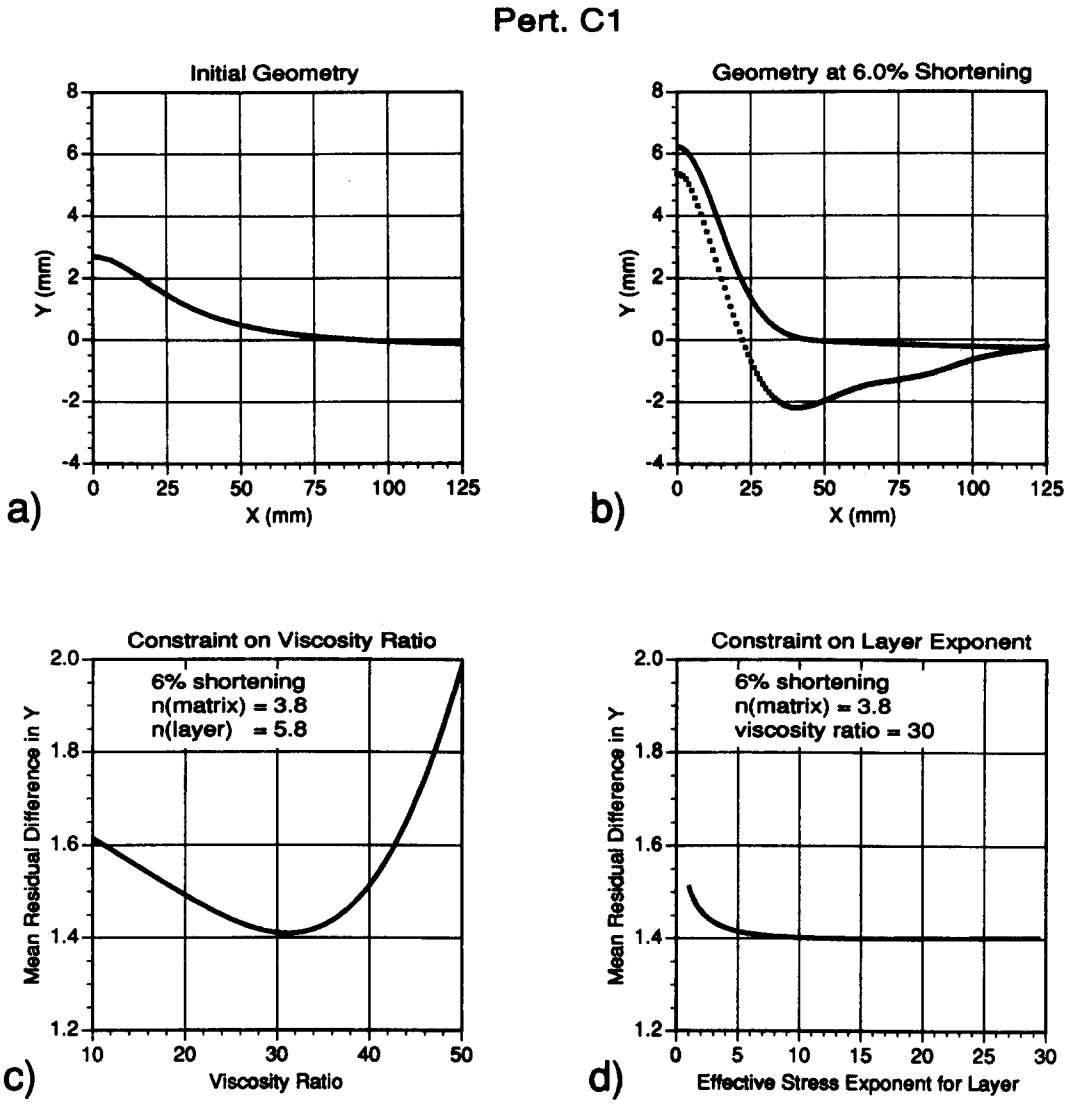

Fig. 12. Results of the best-fit shape analysis for the right side of the fold in experiment Pert C1, with an initial average wavelength to the perturbation of 32 times layer thickness. (a) Best-fit bell-shaped curve to the introduced perturbation. For the degree of exaggeration in Y, the fit is so good that the digitized experimental points are lost in the thickness of the line. (b) Digitized fold shape (points) and best-fit theoretical shape (line) at 6% shortening. (c) Mean residual difference in the Y co-ordinate between theoretical prediction and the observed experimental shape as a function of the viscosity ratio used in the numerical calculation. The minimum value is moderately well constrained at around 30–32, which is very close to the calibrated value of 30. (d) Mean residual difference in the Y co-ordinate between theoretical prediction and the observed experimental shape as a function of the stress exponent for the layer used in the numerical calculation. The minimum value is unconstrained above a value of *ca* 6. This lack of constraint reflects the influence of the initial perturbation shape (see text and Fig. 14).

(1961), using the growth rate equation (1) derived by Fletcher (1974) and Smith (1979), is remarkably good at predicting the material properties from the fold shape, *provided* that the initial perturbation shape is known. As can be seen from Figs. 10–13, it is the viscosity contrast which has the strongest influence on the fold shape, followed by the power-law exponent of the layer. The value of n_L is best constrained for high viscosity contrast and narrow initial perturbations. The reason for this is clear from Fig. 14. At long wavelengths (i.e. low values of layer thickness/wavelength in Fig. 14), the effect of n_L on the growth rate is negligible, especially for larger values of n_L; but it becomes quite significant at shorter wavelengths (Fig. 14a). The broad perturbation Pert C, with average initial wavelength/thickness of 32, has most of its initial Fourier components of significant amplitude in the range where n_L has negligible effect. The value of n_L will, therefore, have little effect on the fold shape developed from such a perturbation and n_L will be poorly constrained by the best-fit shape analysis (Fig. 12d). In contrast, the narrow perturbation Pert A has many of its components in the range of wavelengths where the n_L value exerts a significant effect on the growth rate of individual components. This will be reflected in the fold shape and more tightly constrain the possible values of n_L. For lower viscosity contrast, the wavelength with maximum growth rate is shorter, moving the maximum towards the right in a plot such as Fig. 14(a), and increasing the range of wavelengths where n_L has little influence. In experiments with low viscosity

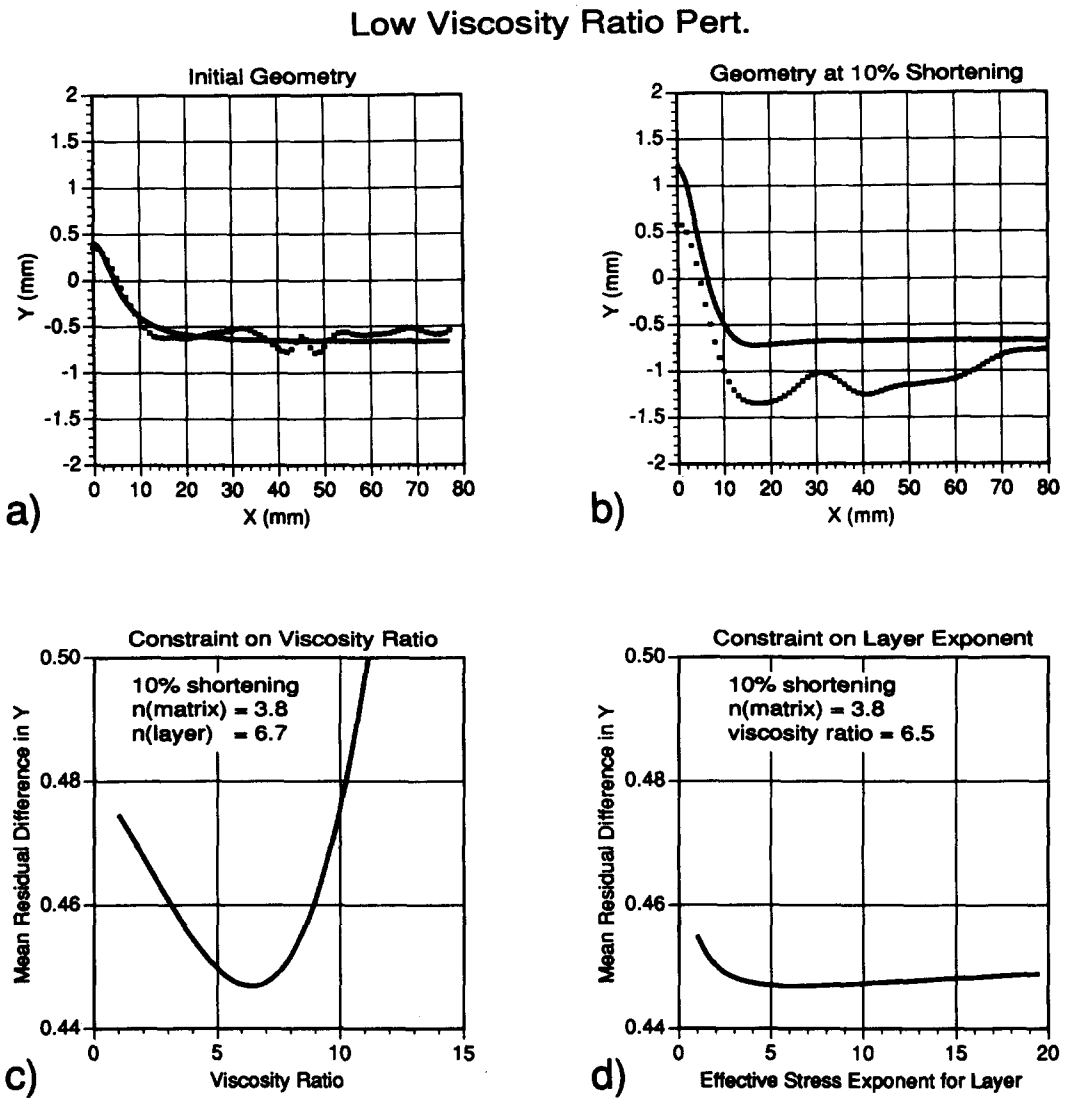

Fig. 13. Results of the best-fit shape analysis for the right side of the fold for the experiment in which the viscosity ratio between layer and matrix was only *ca* 8. (a) Digitized initial shape (points) and best-fit bell-shaped curve (solid line). (b) Digitized fold shape (points) and best-fit theoretical shape (line) at 10% shortening. (c) Mean residual difference in the Y co-ordinate between theoretical prediction and the observed experimental shape as a function of the viscosity ratio used in the numerical calculation. The minimum value is well constrained at around 6.5, which is reasonably close to the calibrated value of *ca* 8. (d) Mean residual difference in the Y co-ordinate between theoretical prediction and the observed experimental shape as a function of the stress exponent for the layer used in the numerical calculation. The minimum value is very weakly constrained around a value of *ca* 6.

contrast, n_L will be more poorly constrained than in experiments with high viscosity contrast but similar initial geometry (Fig. 13).

Although the prediction of material properties is quite good, there is a consistent discrepancy in shape between theoretical prediction and the observed fold geometry, particularly for the broader initial perturbations: the experimental folds are displaced downwards when compared to the theoretical curves (e.g. Fig. 11). This may be a finite shape effect, not considered in the theoretical analysis. The initial introduced perturbation shape is not symmetric about the plane of the layer. It protrudes only to one side of the layer (Figs. 10a, 11a and 12a). During deformation, this antiform amplifies and protrudes still further into the adjacent matrix. In constant volume experiments, however, the volume of matrix to either side of the layer remains unchanged during deformation, and the indentation of the central antiform into the matrix to one side must be compensated. The small flanking synforms are insufficient to provide this compensation, so that the layer as a whole is depressed downwards in a broad synformal depression about the central antiform, as is clearly seen in Figs. 11(b) & (c) and Fig. 12(b). This effect is strongest for the broader perturbations (Pert B and Pert C) because they displace more matrix as they develop than does the narrow perturbation (Pert A). If this effect was eliminated, the degree of fit between experimental folds and theoretically developed folds would be very good.

CONCLUSIONS

The experiments verify that, for low fold amplitudes and correspondingly low limb dips, where the assump-

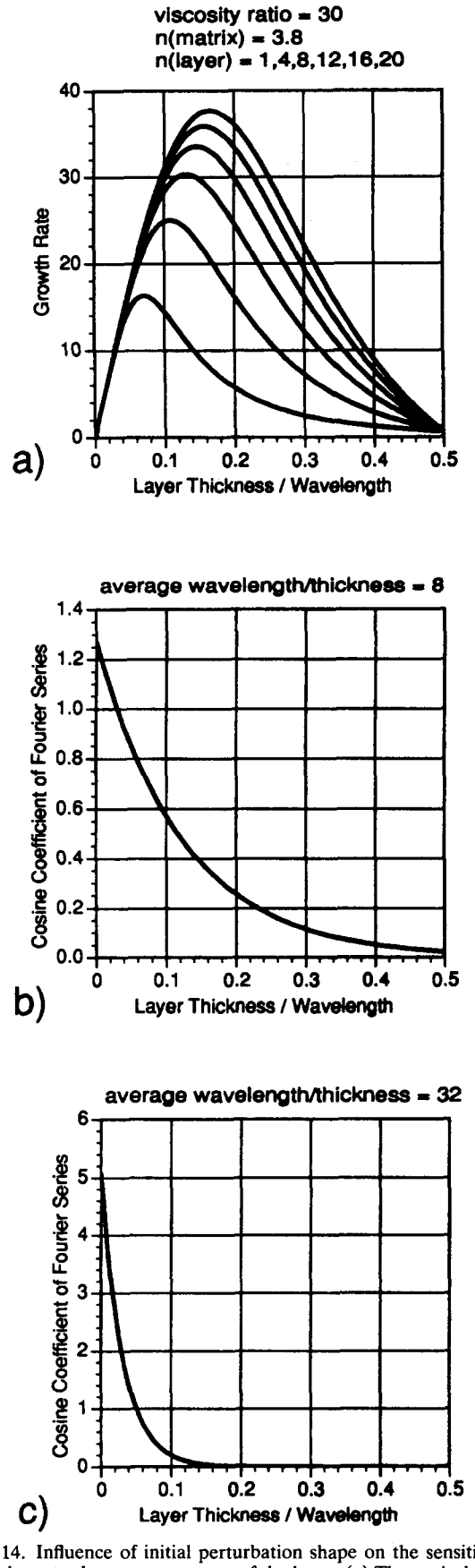

Fig. 14. Influence of initial perturbation shape on the sensitivity of fold shape to the stress exponent of the layer. (a) Theoretical growth rate curves, derived from equation (1), for a fixed viscosity ratio of 30 and stress exponent of the matrix 3.8, but for various values of the stress exponent of the layer. (b) Fourier cosine coefficients for an initial bell-shaped curve with average wavelength 8 times layer thickness. (c) Fourier cosine coefficients for an initial bell-shaped curve with average wavelength 32 times layer thickness.

tions of the infinitesimal fold theories are acceptable, the fit between current non-linear fold theories and experimental observation is good. The results presented here should be considered as a preliminary study which demonstrate the potential of the methods employed. Further experiments are required over a greater range of viscosity ratios and power law exponents, and with analogue materials which flow in steady-state, to more exhaustively test the non-linear fold theories and their extrapolation to small but finite fold amplitudes. The method of Fourier analysis used here is potentially very powerful, in that a range of growth rates for different wavelengths can be determined in a single experiment, whereas experimental studies of sinusoidal folds (e.g. Neurath & Smith 1982) can only determine a single growth rate for one specific wavelength. The assumption in such an approach, namely the superposition principle of independent Fourier components, is intrinsic to the fold theories themselves, and can be tested directly from the linearity of plots of the logarithm of the Fourier coefficients vs logarithmic strain (e.g. Fig. 7). Unfortunately, for non-sinusoidal natural folds (the common situation, cf. plate 1 from Sherwin & Chapple 1968), the amplitude of the fold hinge does not correspond to the amplitude of any particular wavelength component, but represents a superposition of the amplified components from the initial perturbations (see also Part I, Abbassi & Mancktelow 1992). As the exact shape of the initial natural perturbation is unknown and only the final fold shape is available for analysis, neither the progressive Fourier analysis nor the best-fit fold shape analysis can be directly applied to determine material properties in natural folds. Accurately scaled analogue model experiments, which permit a detailed analysis of fold geometry during progressive deformation, help provide a basic understanding of the processes of buckle fold formation, which can be qualitatively applied to natural examples.

Acknowledgements—This paper benefited greatly from very thorough reviews by Peter Cobbold, Raymond Fletcher and Sue Treagus, whose comments were much appreciated. Thanks are also due to John Ramsay for his support for the model deformation laboratory, to Robert Hofmann for invaluable expertise in constructing the deformation rig, and to Martin Casey for many stimulating discussions on buckle fold mechanisms.

REFERENCES

Abbassi, M. R. & Mancktelow, N. S. 1990. The effect of initial perturbation shape and symmetry on fold development. *J. Struct. Geol.* **12**, 273–282.

Abbassi, M. R. & Mancktelow, N. S. 1992. Single layer buckle folding in non-linear materials—I. Experimental study of fold development from an isolated initial perturbation. *J. Struct, Geol.* **13**, 85–104.

Biot, M. A. 1957. Folding instability of a layered viscoelastic medium under compression. *Proc. R. Soc. Lond.* **A242**, 444–454.

Biot, M. A. 1959a. Folding of a layered viscoelastic medium derived from an exact stability theory of a continuum under initial stress. *Appl. Math. Q.* **17**, 185–204.

Biot M. A. 1959b. On the instability and folding deformation of a layered viscoelastic medium in compression. *J. appl. Mech.* **E26**, 393–400.

Biot, M. A. 1959c. The influence of gravity on the folding of a layered viscoelastic medium under compression. *J. Franklin Inst.* **267**, 211–228.

Biot, M. A. 1961. Theory of folding of stratified viscoelastic media and

its implications in tectonics and orogenesis. *Bull. geol. Soc. Am.* **72**, 1595–1620.
Biot, M. A. 1963. Internal buckling under initial stress in finite elasticity. *Proc. R. Soc. Lond.* **A273**, 306–328.
Biot, M. A. 1964a. Theory of internal buckling of a confined multilayered structure. *Bull. geol. Soc. Am.* **75**, 563–568.
Biot, M. A. 1964b. Theory of viscous buckling of multilayered fluids undergoing finite strain. *Physics Fluids* **7**, 855–859.
Biot, M. A. 1965a. Theory of similar folding of the first and second kind. *Bull. geol. Soc. Am.* **76**, 251–258.
Biot, M. A. 1965b. *Mechanics of Incremental Deformations*. John Wiley & Sons, New York.
Biot, M. A. 1965c. Theory of viscous buckling and gravity instability of multilayers with large deformation. *Bull. geol. Soc. Am.* **76**, 371–378.
Biot, M. A., Odé, H. & Roever, W. L. 1961. Experimental verification of the theory of folding of stratified viscoelastic media. *Bull. geol. Soc. Am.* **72**, 1621–1632.
Chapple, W. M. 1968. A mathematical theory of finite-amplitude rock-folding. *Bull. geol. Soc. Am.* **79**, 47–68.
Chapple, W. M. 1969. Fold shape and rheology: the folding of an isolated viscous-plastic layer. *Tectonophysics* **7**, 97–116.
Cobbold. P. R., Cosgrove, J. W. & Summers, J. M. 1971. Development of internal structures. *Tectonophysics* **12**, 23–53.
Cobbold, P. R. 1975. Fold propagation in single embedded layers. *Tectonophysics* **27**, 333–351.
Cobbold, P. R. & Quinquis, H. 1980. Development of sheath folds in shear regime. *J. Struct. Geol.* **2**, 667–677.
Currie, J. B., Patnode, H. W. & Trump, R. P. 1962. Development of folds in sedimentary strata. *Bull. geol. Soc. Am.* **73**, 655–674.
De Caprariis, P. 1974. Stress-induced viscosity changes and the existence of dominant wavelengths in folds. *Tectonophysics* **23**, 139–148.
Dieterich, J. H. 1969. Origin of cleavage in folded rocks. *Am. J. Sci.* **267**, 155–156.
Erzhanov, Z. S. & Egorov, A. K. 1970. The mathematical theory of formation of folds in the earth's crust. *Proc. 2nd Congr. Int. Soc. Rock Mech.* 2–24.
Filon, N. L. 1928. On a quadrature formula for trigonometric integrals. *Proc. R. Soc. Edinb.* **A49**, 38–47.
Fletcher, R. C. 1974. Wavelength selection in the folding of a single layer with power-law rheology. *Am. J. Sci.* **274**, 1029–1043.
Fletcher, R. C. 1977. Folding of a single viscous layer: exact infinitesimal-amplitude solution. *Tectonophysics* **39**, 593–606.
Fletcher, R. C. & Sherwin, J. 1978. Arc lengths of single layer folds: a discussion of the comparison between theory and observation. *Am. J. Sci.* **278**, 1085–1098.
Hamming. R. W. 1962. *Numerical Methods for Scientists and Engineers*. McGraw-Hill, New York.
Hubbert, M. K. 1937. Theory of scale models as applied to the study of geologic structures. *Bull. geol. Soc. Am.* **48**, 1459–1520.
Hudleston, P. J. 1973a. An analysis of 'single layer' folds developed experimentally in viscous media. *Tectonophysics* **16**, 189–214.
Hudleston, P. J. 1973b. The analysis and interpretation of minor folds developed in the Moine rocks of Monar, Scotland. *Tectonophysics* **17**, 89–132.
Hudleston, P. J. 1986. Extracting information from folds in rocks. *J. Geol. Educ.* **34**, 237–245.
Hudleston, P. J. & Holst, T. B. 1984. Strain analysis and fold shape in a limestone layer and implications for layer rheology. *Tectonophysics* **106**, 321–347.
Johnson, A. M. 1977. *Styles of Folding*. Elsevier, Amsterdam.
Kerr, A. D. 1986. On the buckling analyses of embedded layers. *Tectonophysics* **128**, 139–146.
Latham, J.-P. 1985. The influence of nonlinear material properties and resistance to bending on the development of internal structures. *J. Struct. Geol.* **7**, 225–236.
Lewis, R. W. & Williams, J. R. 1978. A finite-element study of fold propagation in a viscous layer. *Tectonophysics* **44**, 263–283.
Lister, G. S. & Williams, P. F. 1983. The partitioning of deformation in flowing rock masses. *Tectonophysics* **92**, 1–33.
Mancktelow, N. S. 1988. The rheology of paraffin wax and is usefulness as an analogue for rocks. *Bull. geol. Instn. Univ. Uppsala* **14**, 181–193.
Nadai, A. 1963. *Theory of Flow and Fracture of Solids*, 2 Vols. McGraw-Hill, New York.
Neurath, C. & Smith, R. B. 1982. The effect of material properties on growth rates of folding and boudinage: experiments with wax models. *J. Struct, Geol.* **4**, 215–229.
Panozzo, R. 1988. Distortion of orientation data introduced by digitizing procedures. *J. Microscopy* **149**, 83–96.
Parrish, D. K. 1973. A non-linear finite element fold model. *Am. J. Sci.* **273**, 318–334.
Press, W. H., Flannery, B. P., Teukolsky, S. A & Vetterling, W. T. 1986. *Numerical Recipes. The Art of Scientific Computing*. Cambridge University Press, Cambridge.
Price, N. J. 1967. The initiation and development of asymmetrical buckle-folds in non-metamorphosed competent sediments. *Tectonophysics* **4**, 173–201.
Ramberg, H. 1959. Evolution of ptygmatic folding. *Norsk. geol. Tidsskr.* **39**, 99–151.
Ramberg, H. 1960. Relationships between length of arc and thickness of ptygmatically folded veins. *Am J. Sci.* **258**, 36–46.
Ramberg, H. 1961. Contact strain and folding instability of a multilayered body under compression. *Geol. Rdsch.* **51**, 405–439.
Ramberg, H. 1963. Fluid dynamics of viscous buckling applicable to folding of layered rocks. *Bull. Am. Ass. Petrol. Geol.* **47**, 484–505.
Ramberg, H. 1964a. Strain distribution and geometry of folds. *Bull. geol. Instn. Univ. Uppsala* **42**, 1–20.
Ramberg, H. 1964b. Selective buckling of composite layers with contrasted rheological properties. *Tectonophysics* **1**, 307–341.
Ramberg, H. 1970a. Folding of laterally compressed multilayers in the field of gravity, 1. *Phys. Earth & Planet. Interiors* **2**, 203–232.
Ramberg, H. 1970b. Folding of laterally compressed multilayers in the field of gravity, 2. Numerical examples. *Phys. Earth & Planet. Interiors* **4**, 83.
Ramberg, H. 1981. *Gravity, Deformation and the Earth's Crust*. Academic Press, London.
Ramsay, J. G. 1967. *Folding and Fracturing of Rocks*. McGraw-Hill, New York.
Ranalli, G. 1987. *Rheology of the Earth*. Allen & Unwin, Boston.
Schmeling, H. 1987. On the interaction between small and large-scale convection and postglacial rebound flow in a power-law mantle. *Earth Planet. Sci. Lett.* **84**, 254–262.
Sherwin, J. & Chapple, W. M. 1968. Wavelengths of single layer folds: a comparison between theory and observation. *Am. J. Sci.* **266**, 167–179.
Singleton, R. C. 1967. On computing the fast Fourier transform. *Comm. ACM* **10**, 647–654.
Smith, R. B. 1975. Unified theory of the onset of folding, boudinage and mullion structure. *Bull. geol. Soc. Am.* **86**, 1601–1609.
Smith, R. B. 1977. Formation of folds, boudinage, and mullions in non-Newtonian materials. *Bull. geol. Soc. Am.* **88**, 312–320.
Smith, R. B. 1979. The folding of a strongly non-Newtonian layer. *Am. J. Sci.* **279**, 272–287.
Suppe, J. 1983. Geometry and kinematics of fault-bend folding. *Am. J. Sci.* **283**, 684–721.
Suppe, J. & Medwedeff, D. A. 1990. Geometry and kinematics of fault-propagation folding. *Eclog. geol. Helv.* **83**, 409–454.
Treagus, S. H. 1973. Buckling instability of a viscous single-layer system, oblique to the principal compression. *Tectonophysics* **19**, 271–289.
Van Den Driessche, J. & Brun J.-P. 1987. Rolling structures at large shear strain. *J. Struct. Geol.* **9**, 691–704.

APPENDIX

Fourier analysis

Consider a real, single-valued sequence of N data values $\{y_j\}$, for $j = 0,1 \ldots N-1$, with N even, which is sampled at discrete, equally spaced values of $x = j\Delta$, where Δ is the sampling interval. The Fourier cosine and sine coefficients, respectively, can be represented as

$$a_k = \frac{2}{N}\sum_{j=0}^{N-1} y_j \cos\left(\frac{2\pi jk}{N}\right) \text{ for } k = 0,1, \ldots, \frac{N}{2}$$

$$b_k = \frac{2}{N}\sum_{j=0}^{N-1} y_j \sin\left(\frac{2\pi jk}{N}\right) \text{ for } k = 1,2, \ldots, \frac{N}{2} - 1.$$

The original sequence of data can be recovered by the inverse relationship

$$y_j = \frac{a_0}{2} + \sum_{k=1}^{N/2-1}\left[a_k \cos\left(\frac{2\pi jk}{N}\right) + b_k \sin\left(\frac{2\pi jk}{N}\right)\right] + \frac{a_{N/2}}{2}$$

for $j = 0,1, \ldots, N-1$

(e.g. Singleton 1967, Hamming, 1962).

The discrete data set has effectively been mapped (i.e. scaled) into the range 0–2π and represented by a series of sine and cosine harmonics. This can be readily seen by considering the term within the brackets of the periodic cosine and sine functions in the above equations, namely $(2\pi jk/N)$. Now, for a constant sampling interval Δ,

$$\frac{j}{N} = \frac{j\Delta}{N\Delta} = \frac{x_j}{x_N} \text{ for } j = 0,1, \ldots . N-1$$

and therefore,

$$\frac{2\pi jk}{N} \equiv \left(\frac{2\pi k}{x_N}\right) x_j = l_k x_j,$$

where l_k = the wavenumber = $(2\pi/L_k)$, and L_k is the wavelength.

Thus,

$$l_k = \frac{2\pi}{L_k} = \frac{2\pi k}{x_N}$$

and $L_k = x_N/k$, where $k = 0,1 \ldots . N/2$ for the cosine coefficients, and $k = 1,2, \ldots . N/2 - 1$ for the sine coefficients.

It also follows that

$$l_{k+1} - l_k = \frac{2\pi(k+1)}{x_N} - \frac{2\pi(k)}{x_N} = \frac{2\pi}{x_N}.$$

In other words, the Fourier components always represent an integer number of wavelengths within the range of x $(x = 0 \ldots x_N)$, and the discrete interval in the wavenumber of each of these components is given by $2\pi/x_N$. This observation is important: the size of the discrete steps in the wavenumber ultimately limits the resolution with which the growth rate curve for experimental folds can be determined (e.g. Fig. 8). The size of the discrete steps is entirely dependent on the length (x_N) of the layer which is digitized from the experiments. It cannot be improved, for example, by decreasing the size of the sampling interval Δ.